

# Breaking $\sum m_\nu$ Parameter Degeneracies with the Bispectrum

CHANGHOON HAHN,<sup>1,2,\*</sup> FRANCISCO VILLAESCUSA-NAVARRO,<sup>3</sup> EMANUELE CASTORINA,<sup>2,1</sup> AND  
ROMAN SCOCCIMARRO<sup>4</sup>

<sup>1</sup>*Lawrence Berkeley National Laboratory, 1 Cyclotron Rd, Berkeley CA 94720, USA*

<sup>2</sup>*Berkeley Center for Cosmological Physics, University of California, Berkeley, CA 94720, USA*

<sup>3</sup>*Center for Computational Astrophysics, Flatiron Institute, 162 5th Avenue, New York, NY 10010, USA*

<sup>4</sup>*Center for Cosmology and Particle Physics, Department of Physics, New York University, NY 10003, New York, USA*

(Dated: DRAFT --- a964c97 --- 2019-03-29 --- NOT READY FOR DISTRIBUTION)

## ABSTRACT

abstract

*Keywords:* cosmology: —

## 1. INTRODUCTION

very brief intro on neutrinos

Brief intro on the impact of massive active neutrinos on the matter powerspectrum and how that’s detectable with CMB and LSS

Quick summary of current constraints and where they come from. Talk about the CMB-LSS lever arm. The degeneracy between  $A_s$  and  $\tau$  and how that’s a bottleneck short thing about how  $\tau$  is hard to constrain.

Fortunately the imprint of neutrinos on the matter distribution leaves imprints on clustering. So with clustering measurements alone we can derive constraints on  $\sum m_\nu$  and at the very least tighten constraints.

Brief summary of previous works that look at the powerspectrum. Then Discuss the shortcomings of the powerspectrum only analysis– Not good enough.

However, we don’t have to settle for just two point statistics, three-point statistics such as the bispectrum and 3PCF...

In Section blah

## 2. HADES AND QUIJOTE SIMULATION SUITES

We use a subset of the HADES<sup>1</sup> and Quijote simulation suites. Below, we briefly describe these simulations; a brief summary of the simulations can be found in Table 1. The HADES simulations start from Zel’dovich approximated initial conditions generated at  $z = 99$  using the [Zennaro](#)

\* hahn.changhoon@gmail.com

<sup>1</sup> <https://franciscovillaescusa.github.io/hades.html>

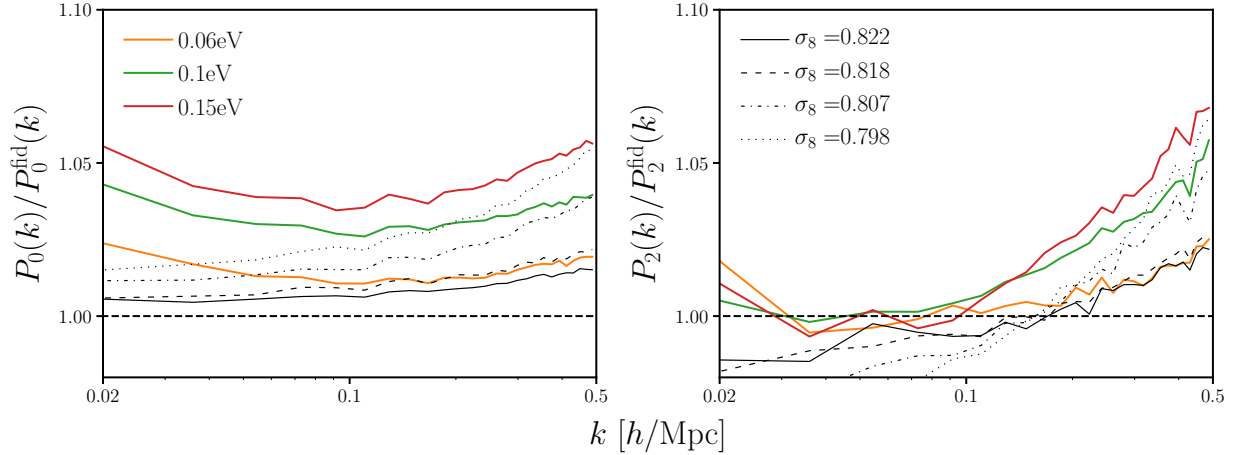


**Figure 1.** Impact of  $\sum m_\nu$  and  $\sigma_8$  on the redshift-space halo power spectrum monopole and quadrupole measured using the HADES simulation suite.  $\sum m_\nu$  and  $\sigma_8$  produce almost identical effects on halo clustering on small scales ( $k > 0.1 h/\text{Mpc}$ ). This degeneracy can be partially broken through the quadrupole; however,  $\sum m_\nu$  and  $\sigma_8$  produce almost the same effect on two-point clustering — within a few percent.

et al. (2017) rescaling method and follow the gravitational evolution of  $N_{\text{cdm}} = 512^3$  CDM, plus  $N_\nu = 512^3$  neutrino particles (for massive neutrino models), to  $z = 0$ . They are run using the GADGET-III TreePM+SPH code (Springel 2005) in a periodic  $(1h^{-1}\text{Gpc})^3$  box. All of the HADES simulations share the following cosmological parameter values, which are in good agreement with Planck constraints Ade et al. (2016):  $\Omega_{\text{m}}=0.3175$ ,  $\Omega_{\text{b}}=0.049$ ,  $\Omega_{\Lambda}=0.6825$ ,  $n_s=0.9624$ ,  $h=0.6711$ , and  $k_{\text{pivot}} = 0.05 h\text{Mpc}^{-1}$ .

The HADES suite includes models with degenerate massive neutrinos of different masses:  $\sum m_\nu = 0.06, 0.10$ , and  $0.15$  eV. These massive neutrino models are run using the “particle method”, where neutrinos are described as a collisionless and pressureless fluid and therefore modeled as particles, same as CDM (Brandbyge et al. 2008; Viel et al. 2010). HADES also includes models with massless neutrino and different values of  $\sigma_8$  to examine the  $\sum m_\nu - \sigma_8$  degeneracy. The  $\sigma_8$  values were chosen to match either  $\sigma_8^m$  or  $\sigma_8^c$  —  $\sigma_8$  computed with respect to total matter (CDM + baryons +  $\nu$ ) or CDM + baryons — of the massive neutrino models:  $\sigma_8 = 0.822, 0.818, 0.807$ , and  $0.798$ . Each model has 100 independent realizations and we focus on the snapshots saved at  $z = 0$ . Halos closely trace the CDM+baryon field rather than the total matter field and neutrinos have negligible contribution to halo masses (e.g. Ichiki & Takada 2012; Castorina et al. 2014; LoVerde 2014; Villaescusa-Navarro et al. 2014). Hence, dark matter halos are identified in each realization using the Friends-of-Friends algorithm (FoF; Davis et al. 1985) with linking length  $b = 0.2$  on the CDM + baryon distribution; only halos with masses  $> 3.2 \times 10^{13} h^{-1} M_\odot$  are included. For further details on the HADES simulations, we refer readers to Villaescusa-Navarro et al. (2018).

**CH:** describe quiote simulations

- describe fixed-pair and state that we tested the bispectrum for fiducial parameter

### 3. BISPECTRUM

**Table 1.** Specifications of the HADES and Quijote simulation suites.

Name	$\sum m_\nu$ (eV)	$\Omega_m$	$\Omega_b$	$h$	$n_s$	$\sigma_8^m$	$\sigma_8^c$	$m_{\text{cdm}}$ ( $10^{10}h^{-1}M_\odot$ )	$m_\nu$ ( $10^{10}h^{-1}M_\odot$ )	realizations
HADES suite										
Fiducial	0.0	0.3175	0.049	0.6711	0.9624	0.833	0.833	65.66	0	100
	0.06	0.3175	0.049	0.6711	0.9624	0.819	0.822	65.36	29.57	100
	0.10	0.3175	0.049	0.6711	0.9624	0.809	0.815	65.16	49.28	100
	0.15	0.3175	0.049	0.6711	0.9624	0.798	0.806	64.92	73.95	100
	0.0	0.3175	0.049	0.6711	0.9624	0.822	0.822	65.66	0	100
	0.0	0.3175	0.049	0.6711	0.9624	0.818	0.818	65.66	0	100
	0.0	0.3175	0.049	0.6711	0.9624	0.807	0.807	65.66	0	100
	0.0	0.3175	0.049	0.6711	0.9624	0.798	0.798	65.66	0	100
Quijote suite										
Fiducial	0.0	0.3175	0.049	0.6711	0.9624	0.834	0.834			15,000
$\sum m_\nu^+$	<u>0.1</u>	0.3175	0.049	0.6711	0.9624	0.834	0.834			500
$\sum m_\nu^{++}$	<u>0.2</u>	0.3175	0.049	0.6711	0.9624	0.834	0.834			500
$\sum m_\nu^{+++}$	<u>0.4</u>	0.3175	0.049	0.6711	0.9624	0.834	0.834			500
$\Omega_m^+$	0.0	<u>0.3275</u>	0.049	0.6711	0.9624	0.834	0.834			500
$\Omega_m^-$	0.0	<u>0.3075</u>	0.049	0.6711	0.9624	0.834	0.834			500
$\Omega_b^+$	0.0	0.3175	<u>0.050</u>	0.6711	0.9624	0.834	0.834			500
$\Omega_b^-$	0.0	0.3175	<u>0.048</u>	0.6711	0.9624	0.834	0.834			500
$h^+$	0.0	0.3175	0.049	<u>0.6911</u>	0.9624	0.834	0.834			500
$h^-$	0.0	0.3175	0.049	<u>0.6511</u>	0.9624	0.834	0.834			500
$n_s^+$	0.0	0.3175	0.049	0.6711	<u>0.9824</u>	0.834	0.834			500
$n_s^-$	0.0	0.3175	0.049	0.6711	<u>0.9424</u>	0.834	0.834			500
$\sigma_8^+$	0.0	0.3175	0.049	0.6711	0.9624	<u>0.849</u>	<u>0.849</u>			500
$\sigma_8^-$	0.0	0.3175	0.049	0.6711	0.9624	<u>0.819</u>	<u>0.819</u>			500

**Notes:** **CH:** description of the table

We're interested in breaking parameter degeneracies that limit the constraining power on  $\sum m_\nu$  of two-point clustering analyses using three-point clustering statistics — *i.e.* the bispectrum. In this section, we describe the bispectrum estimator used throughout the paper. We focus on the bispectrum monopole ( $\ell = 0$ ) and use an estimator that exploits Fast Fourier Transforms (FFTs). Our estimator is similar to the estimators described in [Scoccimarro \(2015\)](#); [Sefusatti et al. \(2016\)](#); we also follow their formalism in our description below. Although [Sefusatti et al. \(2016\)](#) and [Scoccimarro](#)

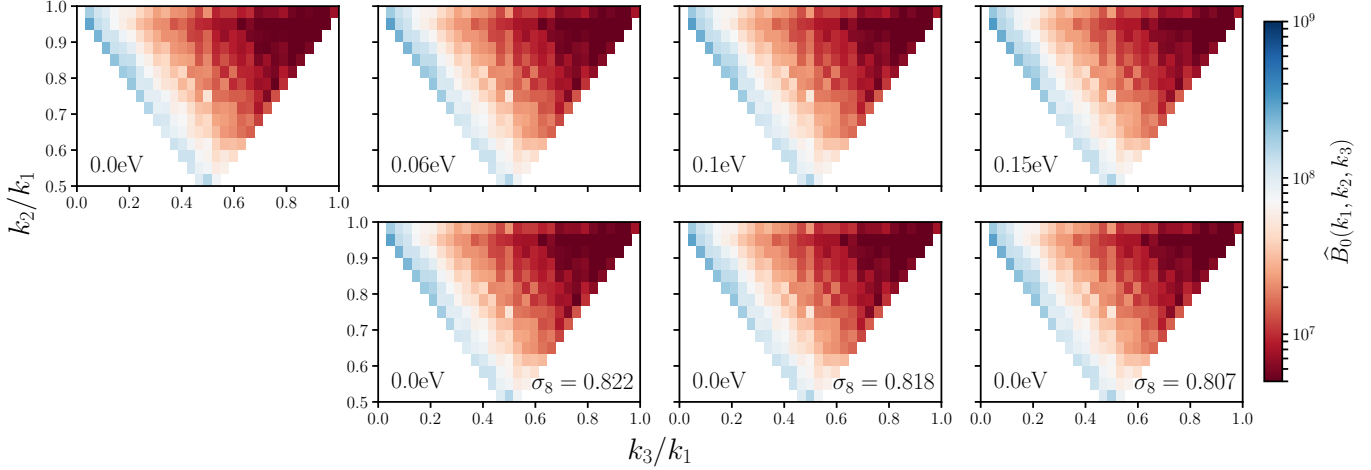


**Figure 2.** The redshift-space halo bispectrum,  $\hat{B}_0(k_1, k_2, k_3)$ , as a function of triangle configuration shape for  $\sum m_\nu = 0.0, 0.06, 0.10$ , and  $0.15$  eV (upper panels) and  $\sigma_8 = 0.822, 0.818$ , and  $0.807$  (lower panels). The HADES simulations of the top and bottom panels in the three right-most columns, have matching  $\sigma_8$  values (Section 2). We describe the triangle configuration shape by the ratio of the triangle sides:  $k_3/k_1$  and  $k_2/k_1$ . The upper left bin contains squeezed triangles ( $k_1 = k_2 \gg k_3$ ); the upper right bin contains equilateral triangles ( $k_1 = k_2 = k_3$ ); and the bottom center bin contains folded triangles ( $k_1 = 2k_2 = 2k_3$ ). We include all triangle configurations with  $k_1, k_2, k_3 \leq k_{\max} = 0.5$   $h/\text{Mpc}$ . and use the  $\hat{B}_0$  estimator in Section 3.

(2015) respectively describe estimators in redshift- and real-space, since we focus on the bispectrum monopole, we note that there is no difference.

To measure the bispectrum of our halo catalogs, we begin by interpolating the halo positions to a grid,  $\delta(\mathbf{x})$  and Fourier transforming the grid to get  $\delta(\mathbf{k})$ . We use a fourth-order interpolation to interlaced grids, which has advantageous anti-aliasing properties (Hockney & Eastwood 1981; Sefusatti et al. 2016) that allow unbiased measurements up to the Nyquist frequency. Then using  $\delta(\mathbf{k})$ , we measure the bispectrum monopole as

$$\hat{B}_{\ell=0}(k_1, k_2, k_3) = \frac{1}{V_B} \int_{k_1} d^3 q_1 \int_{k_2} d^3 q_2 \int_{k_3} d^3 q_3 \delta_D(\mathbf{q}_{123}) \delta(\mathbf{q}_1) \delta(\mathbf{q}_2) \delta(\mathbf{q}_3) - B_{\ell=0}^{\text{SN}} \quad (1)$$

$\delta_D$  above is a Dirac delta function and hence  $\delta_D(\mathbf{q}_{123}) = \delta_D(\mathbf{q}_1 + \mathbf{q}_2 + \mathbf{q}_3)$  ensures that the  $\mathbf{q}_i$  triplet actually form a closed triangle. Each of the integrals above represent an integral over a spherical shell in  $k$ -space with radius  $\delta k$  centered at  $\mathbf{k}_i$  — *i.e.*

$$\int_{k_i} d^3 q \equiv \int_{k_i - \delta k/2}^{k_i + \delta k/2} dq \, q^2 \int d\Omega. \quad (2)$$

$V_B$  is a normalization factor proportional to the number of triplets  $\mathbf{q}_1$ ,  $\mathbf{q}_2$ , and  $\mathbf{q}_3$  that can be found in the triangle bin defined by  $k_1$ ,  $k_2$ , and  $k_3$  with width  $\delta k$ :

$$V_B = \int_{k_1} d^3 q_1 \int_{k_2} d^3 q_2 \int_{k_3} d^3 q_3 \delta_D(\mathbf{q}_{123}) \quad (3)$$

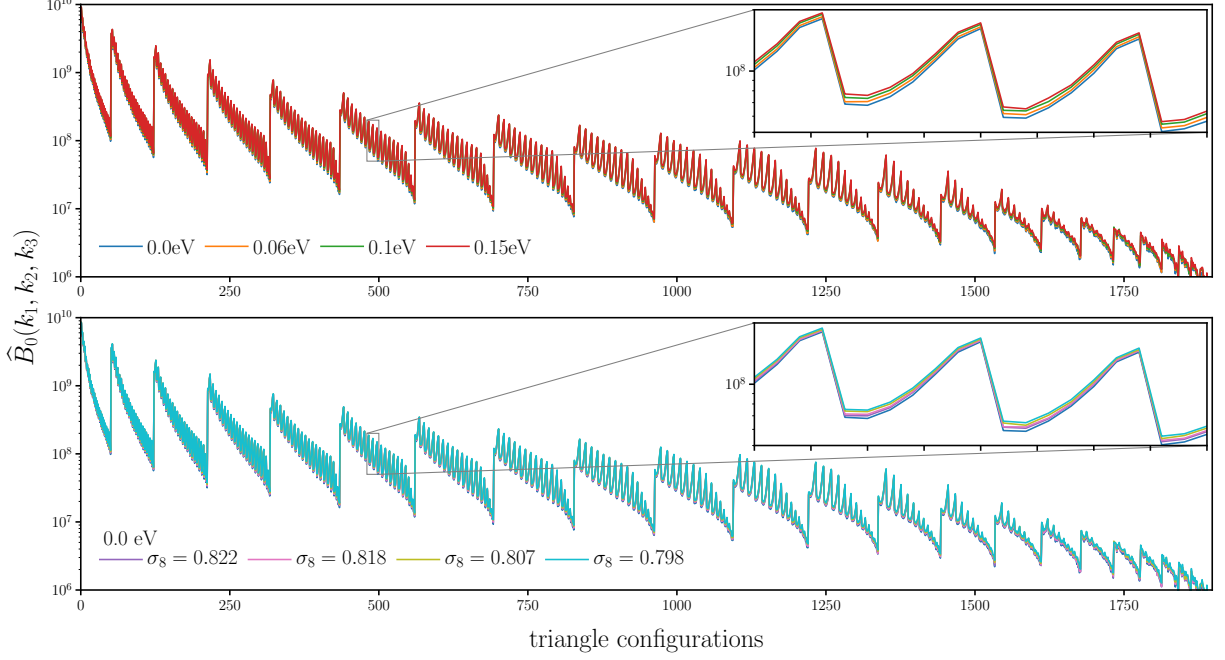


**Figure 3.** The redshift-space halo bispectrum,  $\hat{B}_0(k_1, k_2, k_3)$ , as a function of triangle configurations for  $\sum m_\nu = 0.0, 0.06, 0.10$ , and  $0.15$  eV (top panel) and  $\sum m_\nu = 0.0$  eV,  $\sigma_8 = 0.822, 0.818, 0.807$ , and  $0.798$  (lower panel). We include all possible triangle configurations with  $k_1, k_2, k_3 \leq k_{\max} = 0.5$   $h/\text{Mpc}$  where we order the configurations by looping through  $k_3$  in the inner most loop and  $k_1$  in the outer most loop satisfying  $k_1 \leq k_2 \leq k_3$ . In the insets of the panels we zoom into triangle configurations with  $k_1 = 0.113$ ,  $0.226 \leq k_2 \leq 0.283$ , and  $0.283 \leq k_3 \leq 0.377$   $h/\text{Mpc}$ .

Lastly,  $B_{\ell=0}^{\text{SN}}$  is the correction for the Poisson shot noise, which contributes due to the self-correlation of individual objects:

$$B_{\ell=0}^{\text{SN}}(k_1, k_2, k_3) = \frac{1}{\bar{n}} (P_0(k_1) + P_0(k_2) + P_0(k_3)) + \frac{1}{\bar{n}^2}. \quad (4)$$

$\bar{n}$  is the number density of objects (halos) and  $P_0$  is the powerspectrum monopole.

In order to evaluate the integrals in Eq. 1, we take advantage of the plane-wave representation of the Dirac delta function and rewrite the equation as

$$\hat{B}_{\ell=0}(k_1, k_2, k_3) = \frac{1}{V_B} \int \frac{d^3x}{(2\pi)^3} \int_{k_1} d^3q_1 \int_{k_2} d^3q_2 \int_{k_3} d^3q_3 \delta(\mathbf{q}_1) \delta(\mathbf{q}_2) \delta(\mathbf{q}_3) e^{i\mathbf{q}_{123} \cdot \mathbf{x}} - B_{\ell=0}^{\text{SN}} \quad (5)$$

$$= \frac{1}{V_B} \int \frac{d^3x}{(2\pi)^3} \prod_{i=1}^3 I_{k_i}(\mathbf{x}) - B_{\ell=0}^{\text{SN}} \quad (6)$$

where

$$I_{k_i}(\mathbf{x}) = \int_k d^3q \delta(\mathbf{q}) e^{i\mathbf{q} \cdot \mathbf{x}}. \quad (7)$$

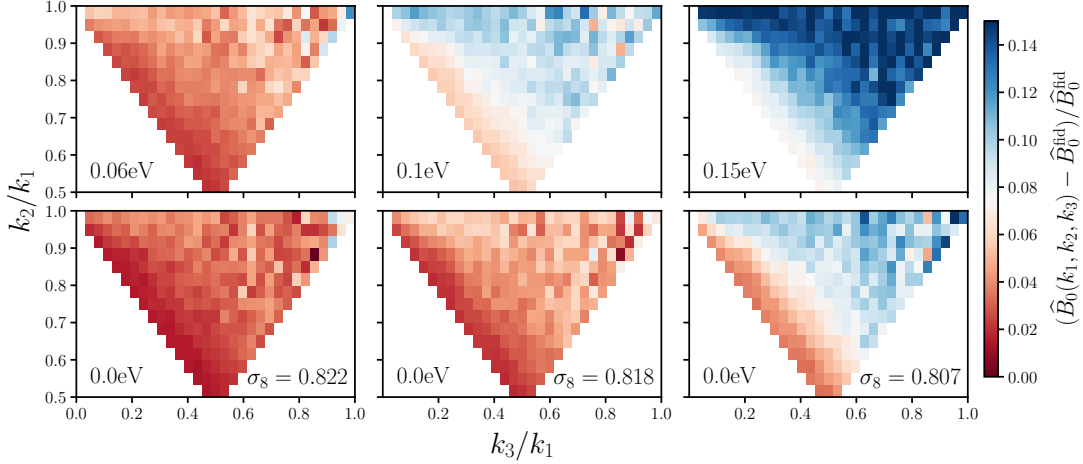


**Figure 4.** The shape dependence of the  $\sum m_\nu$  and  $\sigma_8$  imprint on the redshift-space halo bispectrum,  $\Delta\hat{B}_0/\hat{B}_0^{\text{fid}}$ . We align the  $\sum m_\nu = 0.06, 0.10$ , and  $0.15$  eV HADES models in the upper panels with  $\sum m_\nu = 0.0$  eV  $\sigma_8 = 0.822, 0.818$ , and  $0.807$  models on the bottom such that the top and bottom panels in each column have matching  $\sigma_8^c$ , which produce mostly degenerate imprints on the redshift-space power spectrum. The difference between the top and bottom panels highlight that  $\sum m_\nu$  leaves a distinct imprint on elongated and isosceles triangles (bins along the bottom left and bottom right edges, respectively) from  $\sigma_8$ . *The imprint of  $\sum m_\nu$  has an overall distinct shape dependence on the bispectrum that cannot be replicated by varying  $\sigma_8$ .*

At this point, we measure  $\hat{B}_{\ell=0}(k_1, k_2, k_3)$  by calculating the  $I_{k_i}$ s with inverse FFTs and summing over in real space. For  $\hat{B}_{\ell=0}$  measurements throughout the paper, we use  $\delta(\mathbf{x})$  grids with  $N_{\text{grid}} = 360$  and triangle configurations defined by  $k_1, k_2, k_3$  bins of width  $\Delta k = 3k_f = 0.01885 h/\text{Mpc}$ .

We present the redshift-space halo bispectrum of the HADES simulations measured using the estimator above in two ways: one that emphasizes the triangle shape dependence (Figure 2) and the other that emphasizes the amplitude (Figure 3). In Figure 2, we plot  $\hat{B}_0(k_1, k_2, k_3)$  as a function of  $k_2/k_1$  and  $k_3/k_1$ , which describe the triangle configuration shape. In each panel, the colormap in each  $(k_2/k_1, k_3/k_1)$  bin is the weighted average  $\hat{B}_0$  amplitude of all triangle configurations in the bin. The upper left bins contain squeezed triangles ( $k_1 = k_2 \gg k_3$ ); the upper right bins contain equilateral triangles ( $k_1 = k_2 = k_3$ ); and the bottom center bins contain folded triangles ( $k_1 = 2k_2 = 2k_3$ ). We include all possible triangle configurations with  $k_1, k_2, k_3 < k_{\text{max}} = 0.5 h/\text{Mpc}$ . The  $\hat{B}_0$  in the upper panels are HADES models with  $\sum m_\nu = 0.0$  (fiducial),  $0.06, 0.10$ , and  $0.15$  eV;  $\hat{B}_0$  in the lower panels are HADES models with  $\sum m_\nu = 0.0$  eV and  $\sigma_8 = 0.822, 0.818$ , and  $0.807$ . The top and bottom panels of the three right-most columns have matching  $\sigma_8$  values (Section 2).

Next, in Figure 3, we plot  $\hat{B}_0(k_1, k_2, k_3)$  for all possible triangle configurations with  $k_1, k_2, k_3 < k_{\text{max}} = 0.5 h/\text{Mpc}$  where we order the configurations by looping through  $k_3$  in the inner most loop and  $k_1$  in the outer most loop with  $k_1 \leq k_2 \leq k_3$ . In the top panel, we present  $\hat{B}_0$  of HADES models with  $\sum m_\nu = 0.0, 0.06, 0.10$ , and  $0.15$  eV; in the lower panel, we present  $\hat{B}_0$  of HADES models with  $\sum m_\nu = 0.0$  eV and  $\sigma_8 = 0.822, 0.818$ , and  $0.807$ . We zoom into triangle configurations with  $k_1 = 0.113$ ,  $0.226 \leq k_2 \leq 0.283$ , and  $0.283 \leq k_3 \leq 0.377 h/\text{Mpc}$  in the insets of the panels.

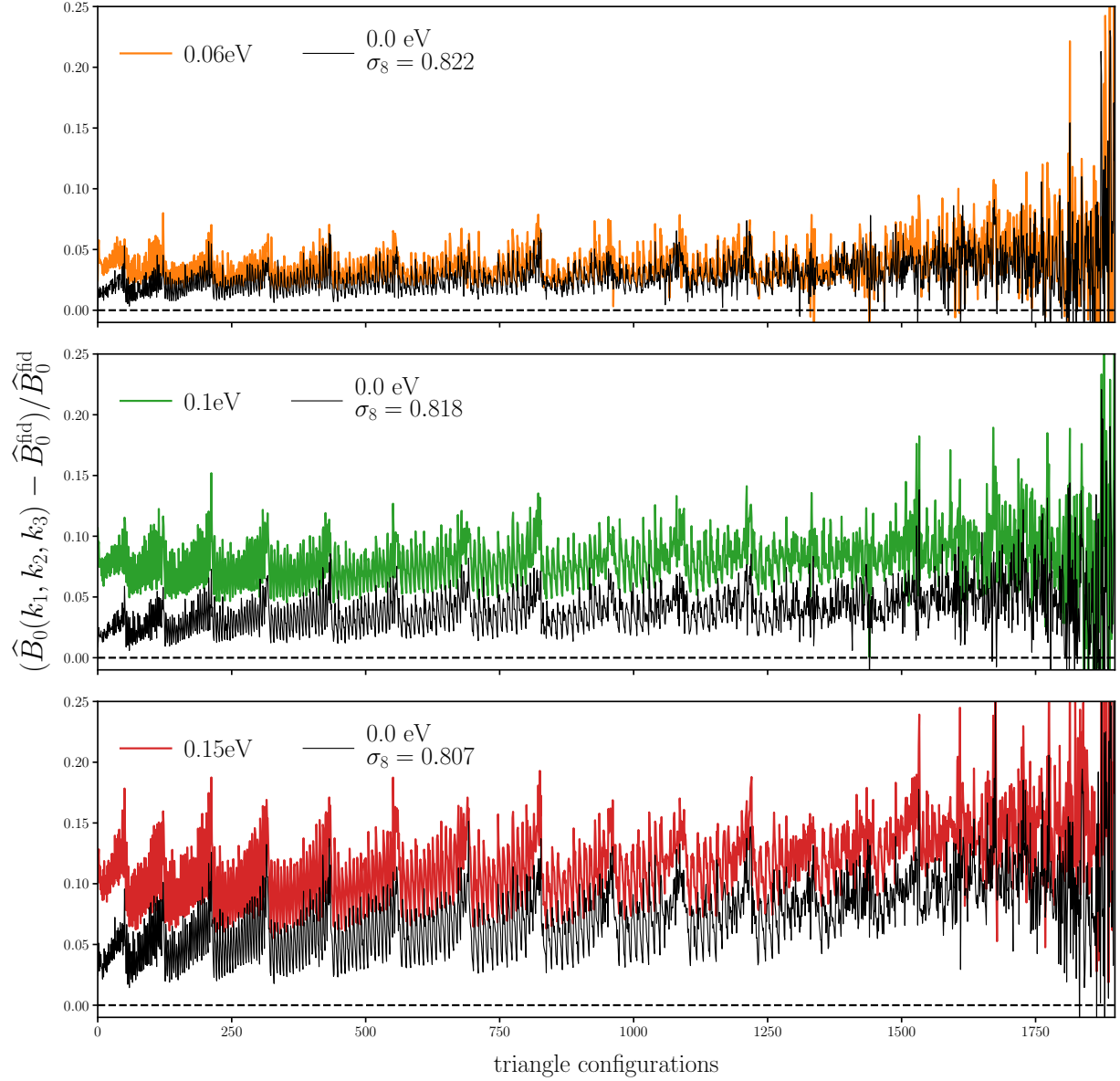


**Figure 5.** The impact of  $\sum m_\nu$  and  $\sigma_8$  on the redshift-space halo bispectrum,  $\Delta\hat{B}_0/\hat{B}_0^{\text{fid}}$ , for all 1898 triangle configurations with  $k_1, k_2, k_3 \leq 0.5h/\text{Mpc}$ . We compare  $\Delta\hat{B}_0/\hat{B}_0^{\text{fid}}$  of the  $\sum m_\nu = 0.06$  (top), 0.10 (middle), and 0.15 eV (bottom) HADES models to  $\Delta\hat{B}_0/\hat{B}_0^{\text{fid}}$  of  $\sum m_\nu = 0.0$  eV  $\sigma_8 = 0.822, 0.818$ , and  $0.807$  models. The impact of  $\sum m_\nu$  on the bispectrum has a significantly different amplitude than the impact of  $\sigma_8$ . For instance,  $\sum m_\nu = 0.15$  eV (red) has a  $\sim 5\%$  stronger impact on the bispectrum than  $\sum m_\nu = 0.0$  eV  $\sigma_8 = 0.798$  (black) even though their powerspectrums only differ by  $< 1\%$  (Figure 1). Combined with the different shape-dependence (Figure 4), the distinct imprint of  $\sum m_\nu$  on the bispectrum illustrate that the bispectrum can break the degeneracy between  $\sum m_\nu$  and  $\sigma_8$  that degrade constraints from two-point analyses.

## 4. RESULTS

### 4.1. Breaking the $\sum m_\nu - \sigma_8$ degeneracy



One major bottleneck of constraining  $\sum m_\nu$  with the power spectrum alone is the strong  $\sum m_\nu - \sigma_8$  degeneracy. The imprint of  $\sum m_\nu$  and  $\sigma_8$  on the power spectrum are degenerate and for models with the same  $\sigma_8^c$ , the power spectrum only differ by  $< 1\%$  (see Figure 1 and Villaescusa-Navarro et al. 2018). The HADES suite, which has simulations with  $\sum m_\nu = 0.0, 0.06, 0.10$ , and  $0.15$  eV as well as  $\sum m_\nu = 0.0$  eV simulations with matching  $\sigma_8^c - \sigma_8 = 0.822, 0.818$ , and  $0.807$ , provide an ideal set of simulations to separate the impact of  $\sum m_\nu > 0.0$  eV and examine the degeneracy between  $\sum m_\nu$  and  $\sigma_8$  (Section 2 and Table 1). Hence, by measuring bispectrum of these simulations (Figure 2 and 3), we can determine whether the bispectrum helps break the  $\sum m_\nu - \sigma_8$  degeneracy. Below, we present our comparison of the HADES bispectrum and illustrate that the bispectrum can significantly improve  $\sum m_\nu$  constraints by breaking the  $\sum m_\nu - \sigma_8$  degeneracy.

We begin by examining the triangle shape dependent imprint of  $\sum m_\nu$  on the redshift-space halo bispectrum versus  $\sigma_8$  alone. In Figure 4, we present the fractional residual,  $(\Delta\hat{B}_0 = \hat{B}_0 - \hat{B}_0^{\text{fid}})/\hat{B}_0^{\text{fid}}$ , as a function of  $k_2/k_1$  and  $k_3/k_1$  for  $\sum m_\nu = 0.06, 0.10$ , and  $0.15$  eV in the upper panels and  $0.0$  eV  $\sigma_8 = 0.822, 0.818$ , and  $0.807$  in the bottom panels. The simulations in the top and bottom panels of each column have matching  $\sigma_8^c$ . Overall as  $\sum m_\nu$  increases, the bispectrum for increases for all triangle shapes (top panels). For triangle shapes close to equilateral (upper right) and squeezed (upper left), the increase is significantly larger. For  $\sum m_\nu = 0.15$  eV, the bispectrum is  $\sim 15\%$  higher than  $\hat{B}_0^{\text{fid}}$  for equilateral and squeezed triangles. Meanwhile, the bispectrum increases by  $\sim 8\%$  for folded triangles (lower center).

As  $\sigma_8$  increases, with  $\sum m_\nu = 0.0$  eV fixed, the bispectrum increases overall for all triangle shapes (bottom panels). However, the comparison of the top and bottom panels in each column reveals significant differences in  $\Delta\hat{B}_0/\hat{B}_0^{\text{fid}}$  for  $\sum m_\nu$  versus  $\sigma_8$  alone. Between  $\sum m_\nu = 0.15$  eV and  $0.0$  eV  $\sigma_8 = 0.807$ , there is an overall  $\gtrsim 5\%$  difference. In addition, the shape dependence of the  $\Delta\hat{B}_0/\hat{B}_0^{\text{fid}}$  increase is different for  $\sum m_\nu$  than  $\sigma_8$ . This is particularly clear in the differences between  $0.1$  eV (top center panel) and  $0.0$  eV and  $\sigma_8 = 0.807$  (bottom right panel): near equilateral triangles in the two panels have similar  $\Delta\hat{B}_0/\hat{B}_0^{\text{fid}}$  while triangle shapes near the lower left edge from the squeezed to folded triangles have significantly different  $\Delta\hat{B}_0/\hat{B}_0^{\text{fid}}$ . Hence,  $\sum m_\nu$  leaves an imprint on the bispectrum with a distinct triangle shape dependence than  $\sigma_8$  alone. In other words, unlike the power spectrum, the triangle shape dependent impact of  $\sum m_\nu$  on the bispectrum cannot be replicated by varying  $\sigma_8$ .

We next examine the amplitude of the  $\sum m_\nu$  imprint on the redshift-space halo bispectrum versus  $\sigma_8$  alone for all triangle configurations. We present  $\Delta\hat{B}_0/\hat{B}_0^{\text{fid}}$  for all 1898 possible triangle configurations with  $k_1, k_2, k_3 < k_{\text{max}} = 0.5 h/\text{Mpc}$  in Figure 5. We compare  $\Delta\hat{B}_0/\hat{B}_0^{\text{fid}}$  of the  $\sum m_\nu = 0.06, 0.10$ , and  $0.15$  eV HADES models to the  $\Delta\hat{B}_0/\hat{B}_0^{\text{fid}}$  of  $\sum m_\nu = 0.0$  eV  $\sigma_8 = 0.822, 0.818$ , and  $0.807$  models in the top, middle, and bottom panels, respectively. The comparison confirms the overall amplitude difference between  $\sum m_\nu$  and  $\sigma_8$  (Figure 4). For instance,  $\sum m_\nu = 0.15$  eV (red) has a  $\sim 5\%$  stronger impact on the bispectrum than  $\sum m_\nu = 0.0$  eV  $\sigma_8 = 0.798$  (black) even though their power spectrums differ by  $< 1\%$  (Figure 1).

The comparison in the panels of Figure 5 also reveal a difference in the configuration dependence in  $\Delta\hat{B}_0/\hat{B}_0^{\text{fid}}$  of  $\sum m_\nu$  versus  $\sigma_8$ . The triangle configurations are ordered by looping through  $k_3$  in the



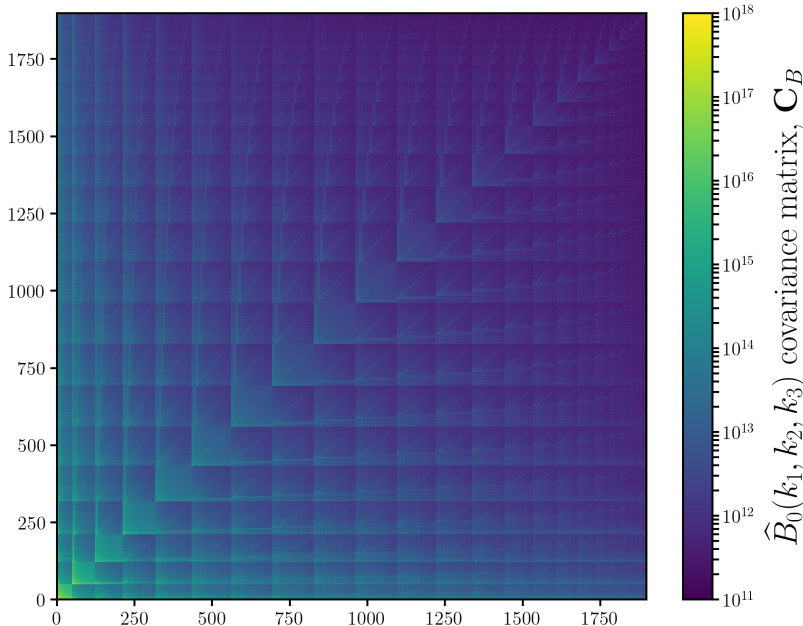


**Figure 6.** Covariance matrix of the redshift-space halo bispectrum estimated using the 15,000 realizations of the Quijote simulation suite at the fiducial cosmology:  $\Omega_m=0.3175$ ,  $\Omega_b=0.049$ ,  $h=0.6711$ ,  $n_s=0.9624$ ,  $\sigma_8=0.834$ , and  $\sum m_\nu=0.0$  eV. We include all possible triangle configurations with  $k_1, k_2, k_3 < k_{\max} = 0.5 h/\text{Mpc}$  and order the configurations (bins) in the same way as Figures 3 and 5. We use the covariance matrix above for the Fisher forecasts of cosmological parameters, including  $\sum m_\nu$ , presented in Section 4.2.

inner most loop and  $k_1$  in the outer most loop such that  $k_1 \leq k_2 \leq k_3$ . In this ordering,  $k_1$  increases from left to right. So  $\Delta \hat{B}_0 / \hat{B}_0^{\text{fid}}$  of  $\sum m_\nu$  has a smaller  $k_1$  dependence than  $\Delta \hat{B}_0 / \hat{B}_0^{\text{fid}}$  of  $\sigma_8$ . Combined with the different shape-dependence (Figure 4), the distinct imprint of  $\sum m_\nu$  on the redshift-space halo bispectrum illustrates that the bispectrum can break the degeneracy between  $\sum m_\nu$  and  $\sigma_8$ . Moreover it illustrates that by including the bispectrum, we can more precisely constrain  $\sum m_\nu$  than with the power spectrum alone.

**CH:** comparison to Ruggeri et al. (2018) and literature

#### 4.2. Forecasts

We demonstrate in the previous section with the HADES simulations, that the bispectrum helps break the  $\sum m_\nu - \sigma_8$  degeneracy, a major challenge in precisely constraining  $\sum m_\nu$  with the power spectrum. This establishes the bispectrum as a promising probe for  $\sum m_\nu$ . However, we are ultimately interested in determining the constraining power of the bispectrum for an analysis that include cosmological parameters beyond  $\sigma_8$  — *i.e.*  $\Omega_m$ ,  $\Omega_b$ ,  $h$ , and  $n_s$ . The Quijote suite of simulations is *specifically* designed to answer this question using Fisher matrix forecast.

First, the Quijote suite includes 15,000 realizations run at a fiducial cosmology:  $\sum m_\nu=0.0\text{eV}$ ,  $\Omega_m=0.3175$ ,  $\Omega_b=0.049$ ,  $n_s=0.9624$ ,  $h=0.6711$ , and  $\sigma_8 = 0.834$  (see Table 1. This allows us to robustly estimate the covariance matrix of the bispectrum,  $\mathbf{C}$ , which has  $\sim 1,800$  triangle configurations (Figure 6). Second, the Quijote suite includes 500 fixed-pair realizations evaluated at 13 cosmologies,

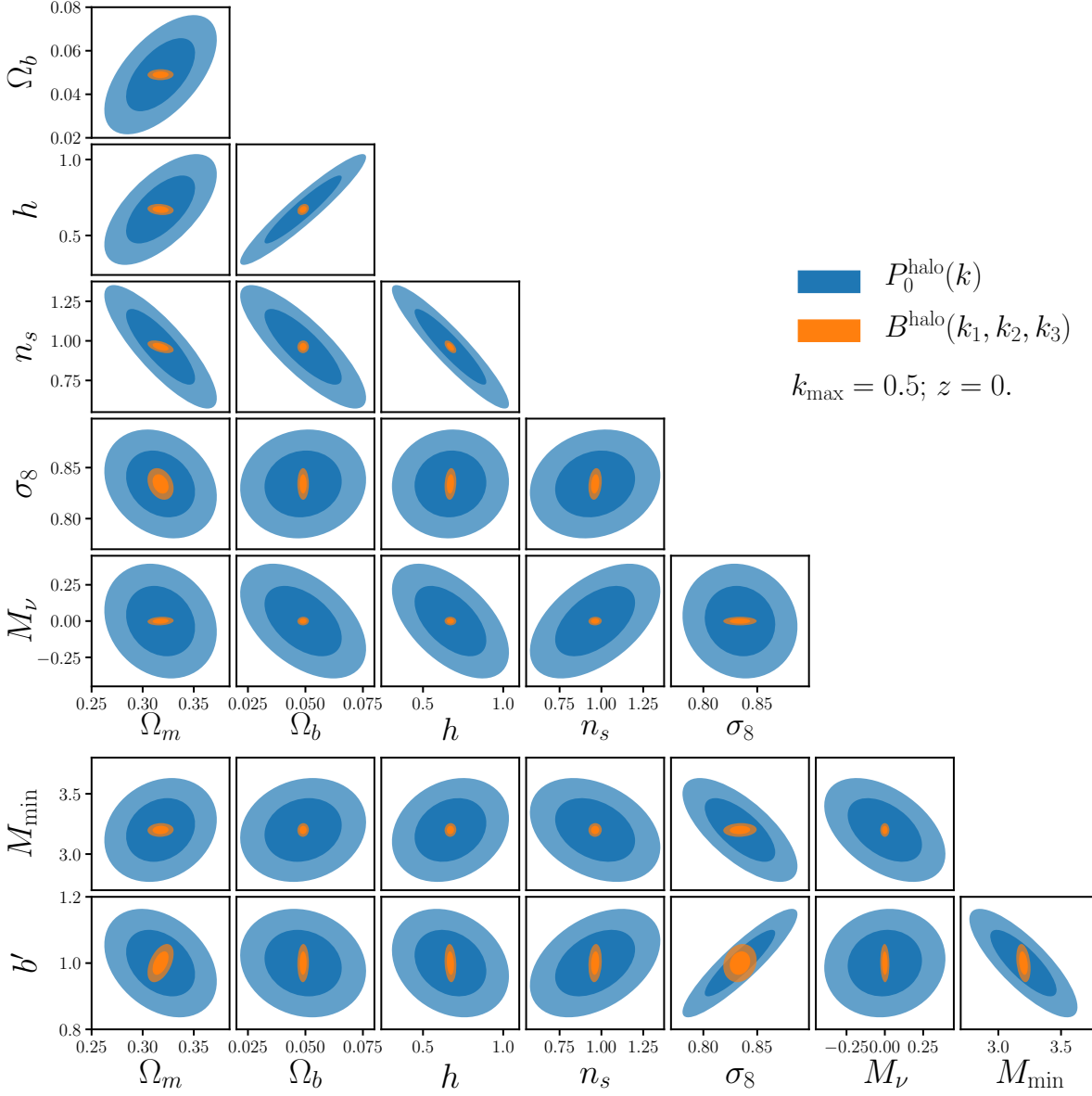


**Figure 7.** Cosmological parameter constraints using the redshift-space halo power spectrum monopole (blue) and bispectrum monopole (orange) forecasted using the Quijote simulation suite. **CH: something about  $b'$  and  $M_{\min}$ .** For both the power spectrum and bispectrum constraints, we set  $k_{\max} = 0.5 \, h/\text{Mpc}$ . The contours mark the 68% and 95% confidence intervals. The bispectrum *substantially* improves constraints on all of the cosmological parameters over the power spectrum. For  $\sum m_\nu$ , the bispectrum improves the constraint from  $\sigma_{\sum m_\nu} = 0.319$  to 0.0239 — over an order of magnitude improvement over the power spectrum.

each a small step away from the fiducial cosmology parameter values along one parameter (underlined values in Table 1). These realizations allow us to precisely estimate the derivatives of the bispectrum with respect to each of the cosmological parameters.

Since their introduction to cosmology over two decades ago, Fisher Information matrices have been ubiquitously used to forecast the constraining power of future experiments (Jungman et al.

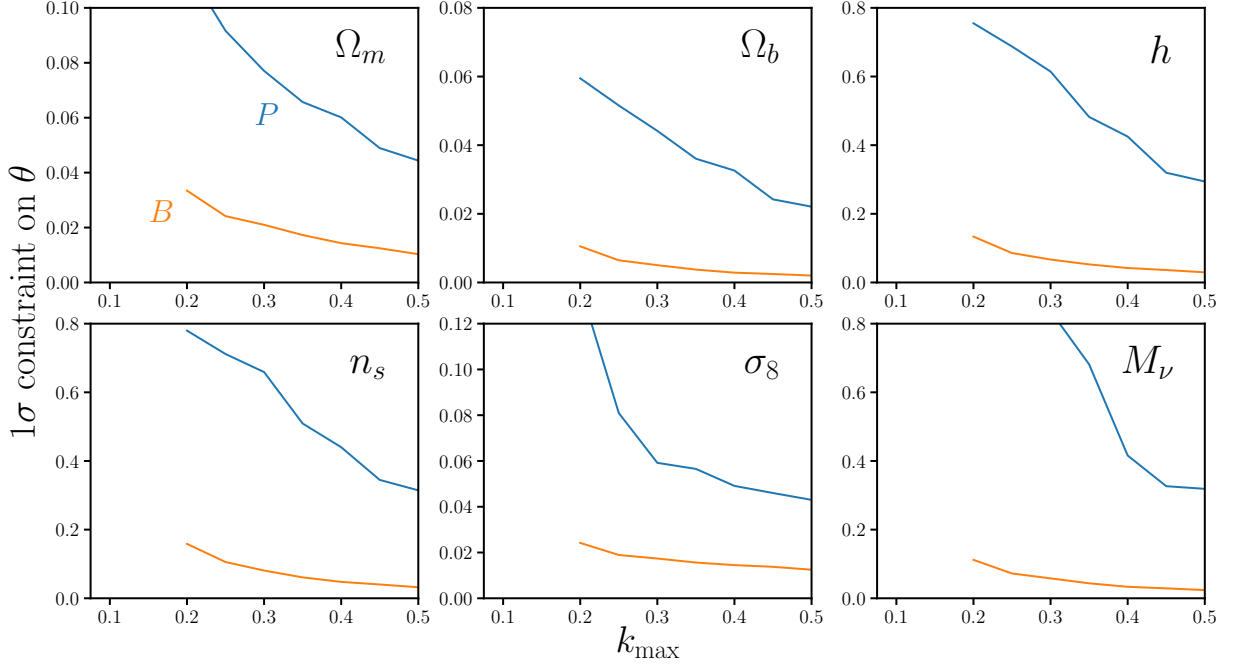


**Figure 8.**  $1\sigma$  Fisher forecast constraints on cosmological parameters as a function of  $k_{\max}$  using the redshift-space halo power spectrum monopole (blue) and bispectrum (orange).

1996; Tegmark et al. 1997; Dodelson 2003; Heavens 2009; Verde 2010). Defined as

$$F_{ij} = -\left\langle \frac{\partial^2 \ln \mathcal{L}}{\partial \theta_i \partial \theta_j} \right\rangle, \quad (8)$$

where  $\mathcal{L}$  is the likelihood, the Fisher matrix for the bispectrum can be written as

$$F_{ij} = \frac{1}{2} \text{Tr} \left[ \mathbf{C}^{-1} \frac{\partial \mathbf{C}}{\partial \theta_i} \mathbf{C}^{-1} \frac{\partial \mathbf{C}}{\partial \theta_j} + \mathbf{C}^{-1} \left( \frac{\partial \bar{B}_0}{\partial \theta_i} \frac{\partial \bar{B}_0}{\partial \theta_j} + \frac{\partial \bar{B}_0}{\partial \theta_i} \frac{\partial \bar{B}_0}{\partial \theta_j} \right) \right]. \quad (9)$$

Since we assume that the  $B_0$  likelihood is Gaussian, including the first term in Eq. 9 runs the risk of incorrectly including information from the covariance already included in the mean (Carron 2013). We, therefore, conservatively neglect the first term and calculate the Fisher matrix as

$$F_{ij} = \frac{1}{2} \text{Tr} \left[ \mathbf{C}^{-1} \left( \frac{\partial \bar{B}_0}{\partial \theta_i} \frac{\partial \bar{B}_0}{\partial \theta_j} + \frac{\partial \bar{B}_0}{\partial \theta_i} \frac{\partial \bar{B}_0}{\partial \theta_j} \right) \right]. \quad (10)$$

With  $\mathbf{C}$  and  $B_0$  derivatives along the cosmological parameters derived directly from the Quijote simulations, calculating  $F_{ij}$  is straightforward.

**CH:** mention the caveats of fisher forecasts

## 5. SUMMARY

## ACKNOWLEDGEMENTS

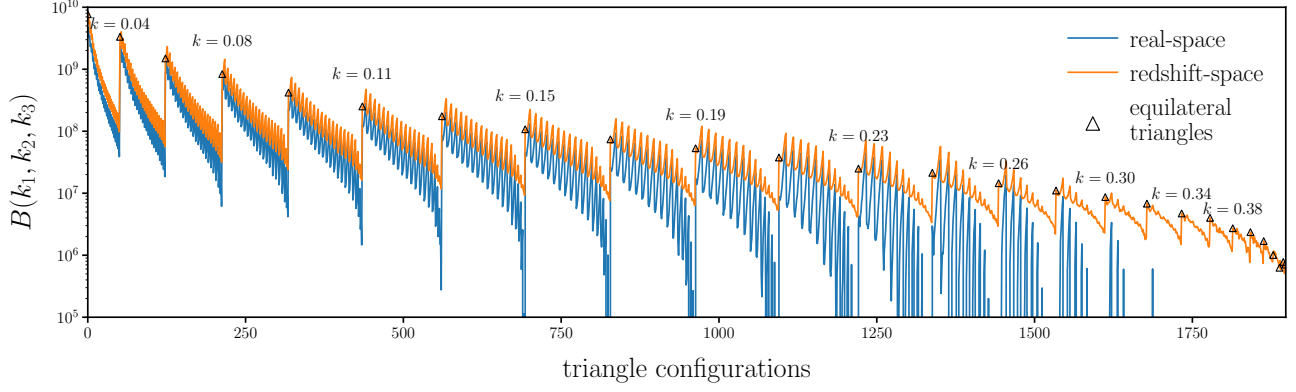


**Figure 9.** Comparison of the fiducial HADES simulations real and redshift-space halo bispectrum for triangle configurations with  $k_1, k_2, k_3 \leq k_{\max} = 0.5h/\text{Mpc}$  (blue and orange respectively). We mark equilateral triangle configurations (empty triangle marker) along with their side lengths  $k$ .

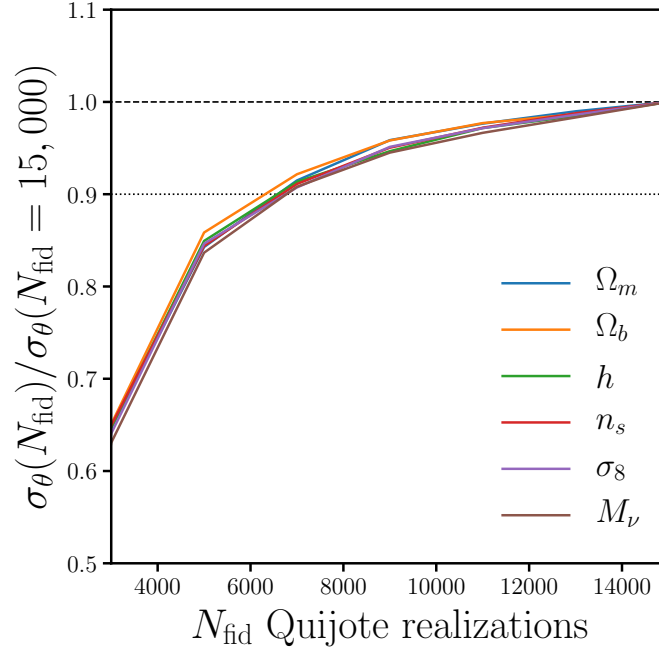


**Figure 10.**

It's a pleasure to thank Daniel Eisenstein, Simone Ferraro, Shirley Ho, Emmaneul Schaan, David N. Spergel, Benjamin D. Wandelt

## APPENDIX

### A. REDSHIFT-SPACE BISPECTRUM

### B. TESTING CONVERGENCE

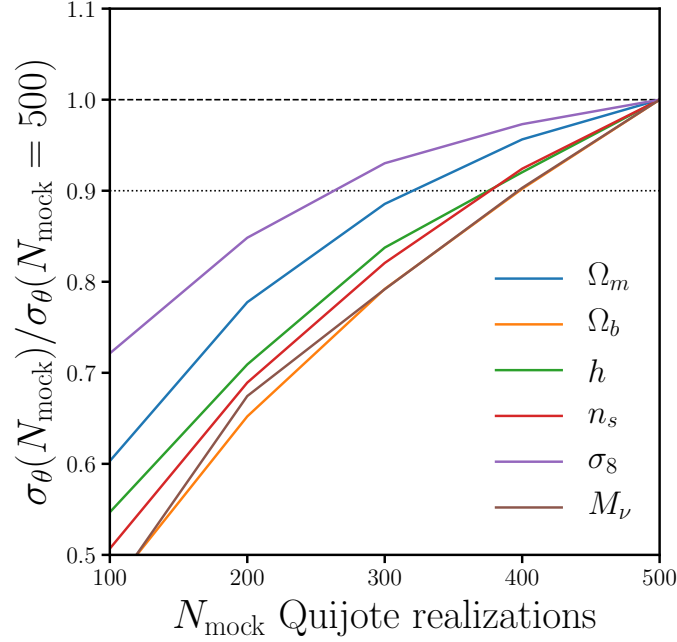


Figure 11.

## REFERENCES

- Ade, P. a. R., Aghanim, N., Arnaud, M., et al. 2016, *Astronomy & Astrophysics*, 594, A13
- Brandbyge, J., Hannestad, S., Haugbølle, T., & Thomsen, B. 2008, *Journal of Cosmology and Astro-Particle Physics*, 08, 020
- Carron, J. 2013, *Astronomy & Astrophysics*, 551, A88
- Castorina, E., Sefusatti, E., Sheth, R. K., Villaescusa-Navarro, F., & Viel, M. 2014, *Journal of Cosmology and Astro-Particle Physics*, 02, 049
- Davis, M., Efstathiou, G., Frenk, C. S., & White, S. D. M. 1985, *The Astrophysical Journal*, 292, 371
- Dodelson, S. 2003, *Modern Cosmology*
- Heavens, A. 2009, arXiv:0906.0664 [astro-ph], arXiv:0906.0664 [astro-ph]
- Hockney, R. W., & Eastwood, J. W. 1981, *Computer Simulation Using Particles*
- Ichiki, K., & Takada, M. 2012, *Physical Review D*, 85, 063521
- Jungman, G., Kamionkowski, M., Kosowsky, A., & Spergel, D. N. 1996, *Physical Review D*, 54, 1332
- LoVerde, M. 2014, *Physical Review D*, 90, 083518
- Scoccimarro, R. 2015, *Physical Review D*, 92, arXiv:1506.02729
- Sefusatti, E., Crocce, M., Scoccimarro, R., & Couchman, H. M. P. 2016, *Monthly Notices of the Royal Astronomical Society*, 460, 3624
- Springel, V. 2005, *Monthly Notices of the Royal Astronomical Society*, 364, 1105
- Tegmark, M., Taylor, A. N., & Heavens, A. F. 1997, *The Astrophysical Journal*, 480, 22
- Verde, L. 2010, arXiv:0911.3105 [astro-ph], 800, 147
- Viel, M., Haehnelt, M. G., & Springel, V. 2010, *Journal of Cosmology and Astro-Particle Physics*, 06, 015
- Villaescusa-Navarro, F., Banerjee, A., Dalal, N., et al. 2018, *The Astrophysical Journal*, 861, 53
- Villaescusa-Navarro, F., Marulli, F., Viel, M., et al. 2014, *Journal of Cosmology and Astro-Particle Physics*, 03, 011
- Zennaro, M., Bel, J., Villaescusa-Navarro, F., et al. 2017, *Monthly Notices of the Royal Astronomical Society*, 466, 3244